The Astronomical Journal, 163:9 (15pp), 2022 January https://doi.org/10.3847/1538-3881/ac2ee1

Two Massive Jupiters in Eccentric Orbits from the TESS Full-frame Images

Mma Ikwut-Ukwa[1], Joseph E. Rodriguez[2], Samuel N. Quinn[1], George Zhou[1], Andrew Vanderburg[3], Asma Ali[1,4], Katya Bunten[1,5], B. Scott Gaudi[6], David W. Latham[1], Steve B. Howell[7], Chelsea X. Huang[8,33], Allyson Bieryla[1], Karen A. Collins[1], Theron W. Carmichael[1,9], Markus Rabus[10,11,12], Jason D. Eastman[1], Kevin I. Collins[13], Thiam-Guan Tan[14,15], Richard P. Schwarz[16], Gordon Myers[17], Chris Stockdale[18], John F. Kielkopf[19], Don J. Radford[20], Ryan J. Oelkers[21], Jon M. Jenkins[7], George R. Ricker[8], Sara Seager[8,22,23], Roland K. Vanderspek[8], Joshua N. Winn[24], Jennifer Burt[25], R. Paul Butler[26], Michael L. Calkins[1], Jeffrey D. Crane[27], Crystal L. Gnilka[7], Gilbert A. Esquerdo[1], William Fong[8], Laura Kreidberg[28], Jessica Mink[1], David R. Rodriguez[29], Joshua E. Schlieder[30,31], Stephen Shectman[27], Avi Shporer[8], Johanna Teske[26], Eric B. Ting[7], Jesus Noel Villaseñor[8], and Daniel A. Yahalomi[1,32]

[1] The Center for Astrophysics | Harvard & Smithsonian, 60 Garden Street, Cambridge, MA 02138, USA; mma.ikwut-ukwa@cfa.harvard.edu
[2] Department of Physics and Astronomy, Michigan State University, East Lansing, MI 48824, USA
[3] Department of Astronomy, University of Wisconsin-Madison, Madison, WI 53706, USA
[4] Algonquin Regional High School, Northborough, MA, USA
[5] Cambridge Rindge and Latin High School, Cambridge, MA, USA
[6] Department of Astronomy, The Ohio State University, 140 West 18th Avenue, Columbus, OH 43210, USA
[7] NASA Ames Research Center, Moffett Field, CA 94035, USA
[8] Department of Physics and Kavli Institute for Astrophysics and Space Research, Massachusetts Institute of Technology, Cambridge, MA 02139, USA
[9] Harvard University, Cambridge, MA 02138, USA
[10] Las Cumbres Observatory Global Telescope, 6740 Cortona Drive, Suite 102, Goleta, CA 93111, USA
[11] Department of Physics, University of California, Santa Barbara, CA 93106-9530, USA
[12] Departamento de Matemática y Fı'sica Aplicadas, Universidad Católica de la Santísima Concepción, Alonso de Rivera 2850, Concepción, Chile
[13] George Mason University, 4400 University Drive, MS 3F3, Fairfax, VA 22030, USA
[14] Perth Exoplanet Survey Telescope, Perth, Australia
[15] Curtin Institute of Radio Astronomy, Curtin University, Bentley 6102, Western Australia
[16] Patashnick Voorheesville Observatory, Voorheesville, NY 12186, USA
[17] American Association of Variable Star Observers, 49 Bay State Road, Cambridge, MA 02138, USA
[18] Hazelwood Observatory, Churchill, Victoria, Australia
[19] Department of Physics and Astronomy, University of Louisville, Louisville, KY 40292, USA
[20] Brierfield Observatory, New South Wales, Australia
[21] Department of Physics and Astronomy, Vanderbilt University, Nashville, TN 37235, USA
[22] Department of Earth, Atmospheric and Planetary Sciences, Massachusetts Institute of Technology, Cambridge, MA 02139, USA
[23] Department of Aeronautics and Astronautics, MIT, 77 Massachusetts Avenue, Cambridge, MA 02139, USA
[24] Department of Astrophysical Sciences, Princeton University, 4 Ivy Lane, Princeton, NJ 08544, USA
[25] Jet Propulsion Laboratory, California Institute of Technology, 4800 Oak Grove Drive, Pasadena, CA 91109, USA
[26] Earth & Planets Laboratory, Carnegie Institution for Science, 5241 Broad Branch Road, NW, Washington, DC 20015, USA
[27] The Observatories of the Carnegie Institution for Science, 813 Santa Barbara Street, Pasadena, CA 91101, USA
[28] Max-Planck-Institut für Astronomie, Königstuhl 17, Heidelberg D-69117, Germany
[29] Space Telescope Science Institute, Baltimore, MD 21218, USA
[30] Exoplanets and Stellar Astrophysics Laboratory, Code 667, NASA Goddard Space Flight Center, Greenbelt, MD 20771, USA
[31] GSFC Sellers Exoplanet Environments Collaboration, NASA Goddard Space Flight Center, Greenbelt, MD 20771, USA
[32] Department of Astronomy, Columbia University, 550 West 120th Street, New York, NY 10027, USA
Received 2021 February 3; revised 2021 September 3; accepted 2021 September 14; published 2021 December 13

Abstract

We report the discovery of two short-period massive giant planets from NASA's Transiting Exoplanet Survey Satellite (TESS). Both systems, TOI-558 (TIC 207110080) and TOI-559 (TIC 209459275), were identified from the 30 minute cadence full-frame images and confirmed using ground-based photometric and spectroscopic follow-up observations from TESS's follow-up observing program working group. We find that TOI-558 b, which transits an F-dwarf ($M_* = 1.349^{+0.064}_{-0.065}$ $M_\odot$, $R_* = 1.496^{+0.042}_{-0.040}$ $R_\odot$, $T_{\rm eff} = 6466^{+95}_{-93}$ K, age $1.79^{+0.91}_{-0.73}$ Gyr) with an orbital period of 14.574 days, has a mass of 3.61 ± 0.15 $M_{\rm J}$, a radius of $1.086^{+0.041}_{-0.038}$ $R_{\rm J}$, and an eccentric ($e = 0.300^{+0.022}_{-0.020}$) orbit. TOI-559 b transits a G dwarf ($M_* = 1.026 \pm 0.057$ $M_\odot$, $R_* = 1.233^{+0.028}_{-0.026}$ $R_\odot$, $T_{\rm eff} = 5925^{+85}_{-76}$ K, age $6.8^{+2.5}_{-2.0}$ Gyr) in an eccentric ($e = 0.151 \pm 0.011$) 6.984 days orbit with a mass of $6.01^{+0.24}_{-0.23}$ $M_{\rm J}$ and a radius of $1.091^{+0.028}_{-0.025}$ $R_{\rm J}$. Our spectroscopic follow up also reveals a long-term radial velocity trend for TOI-559, indicating a long-period companion. The statistically significant orbital eccentricity measured for each system suggests that these planets migrated to their current location through dynamical interactions. Interestingly, both planets are also massive (>3 $M_{\rm J}$), adding to the population of massive giant planets identified by TESS. Prompted by these new

[33] Juan Carlos Torres Fellow.

detections of high-mass planets, we analyzed the known mass distribution of hot and warm Jupiters but find no significant evidence for multiple populations. TESS should provide a near magnitude-limited sample of transiting hot Jupiters, allowing for future detailed population studies.

Unified Astronomy Thesaurus concepts: Hot Jupiters (753); Exoplanets (498); Extrasolar gaseous planets (2172); Exoplanet astronomy (486); Transit photometry (1709); Photometry (1234); Exoplanet detection methods (489); Radial velocity (1332); Direct imaging (387)

Supporting material: data behind figure

1. Introduction

The formation and migration of giant planets in close orbits has been debated extensively. Hot Jupiters (with orbital periods less than 10 days) could theoretically form in a number of ways, with three main formation and migration schemes dominating the literature. It has traditionally been thought that short-period giant planets must form at larger orbital radii and migrate inwards over time (Lin et al. 1996; Rafikov 2006; Dawson & Johnson 2018). In order for the formation outcome to be a giant planet, the core needs to form rapidly enough to accrete gas within the lifetime of the proto-planetary disk (Bodenheimer & Pollack 1986). Core accretion theories suggest that this atmospheric accretion can only occur in a region of the disk where the core can coalesce enough material to grow to ∼10 Earth masses—this critical mass declines as a function of semimajor axis (Piso et al. 2015). This assumes that the mass of the gaseous envelope becomes greater than the mass of the core (Pollack et al. 1996). After formation, a giant planet could migrate to a close-in orbit through either gentle migration through the gas disk (Goldreich & Tremaine 1980; Lin & Papaloizou 1986; Lin et al. 1996) or more dynamical migration caused by interaction with another planet or star (Rasio & Ford 1996; Wu & Murray 2003; Fabrycky & Tremaine 2007; Nagasawa & Ida 2011; Wu & Lithwick 2011), after which the planet's orbit could be circularized and shrunk by tidal forces (Naoz et al. 2011; Beaugé & Nesvorný 2012). However, more recent models have suggested that hot Jupiters may also form in situ (Batygin et al. 2016) and show that the period–mass distribution and inner boundary of short-period giant planets could be consistent with predictions for in situ formation (Bailey & Batygin 2018). Other efforts have shown this mass distribution of giant planets to be consistent with high eccentricity migration from dynamical interaction (Matsakos & Königl 2016). The dominance of each of these three formation and migration scenarios remains an open question, and it is likely that a combination of these methods have shaped the hot Jupiter population seen today. Atmospheric characterization is one frontier that may constrain hot Jupiter migration; the measurement of carbon and oxygen abundances in hot Jupiters can be used to trace migration histories (Madhusudhan et al. 2014).

The discovery of very massive giant planets ($>6\ M_{\rm J}$),[34] has raised the question of whether there are meaningful mass boundaries separating giant planets, brown dwarfs, and low-mass stars—specifically, whether there is a particular mass range in which the dominant formation mechanism changes from core accretion to gravitational instability and fragmentation of giant molecular gas clouds. Some studies (e.g., Schlaufman 2018; Moe & Kratter 2019) have argued that core accretion is the dominant formation mechanism for giant planet companions with masses $M_P < 5\,M_{\rm J}$. Additionally, Schlaufman (2018) notes that higher host-star metallicity is the property associated with core accretion and may indicate that $M_P < 5\,M_{\rm J}$ giant planets may preferentially form via core accretion around metal-rich stars. There also exists a gap in the mass distribution of giant planets very near the threshold of $M_P = 7\,M_{\rm J}$ that Moe & Kratter (2019) claim to be a feasible lower mass boundary for disk fragmentation to form an object. Moe & Kratter (2019) also highlight that relatively metal-poor host stars seem to preferentially host objects at masses at and above this $M_P = 7\,M_{\rm J}$ threshold. The discovery and characterization of massive giant planets and low-mass brown dwarfs may enable a better understanding of the transition between these formation mechanisms.

The observed parameters of a planet and its orbit may be indicative of its formation and migration mechanism. One possible path to determining the dominant mechanism of giant planet migration is to create a complete sample of hot Jupiters with well characterized fundamental parameters (masses and radii, and orbital periods and eccentricities). Statistical population studies of such a sample may provide insight into the dominant evolutionary pathways for giant planets; this type of analysis led to the discovery of the radius valley in small planets (Fulton et al. 2017; Fulton & Petigura 2018), supporting the prediction due to photoevaporation of volatiles (Yelle 2004; Tian et al. 2005; Murray-Clay et al. 2009; Owen & Jackson 2012; Lopez & Fortney 2013).

NASA's Transiting Exoplanet Survey Satellite (TESS), launched in 2018, is an all-sky photometric survey with the goal of discovering thousands of new planets around bright, nearby stars (Ricker et al. 2015). The TESS mission has already discovered over a dozen new hot Jupiters, including a few massive systems ($>3\ M_{\rm J}$ Rodriguez et al. 2019a, 2021; Nielsen et al. 2020), and is expected to be largely complete for giant planets with periods up to 10 days around bright stars (Zhou et al. 2019). Detailed characterization of new discoveries from TESS will help complete the sample of known short-period giant planets, setting the foundation for more robust population studies.

In this paper, we confirm and characterize two short-period giant planets from TESS, TOI-558 b and TOI-559 b. We present the photometric and spectroscopic observations from TESS and ground-based facilities in Section 2, which we globally model using `EXOFASTv2` (Eastman et al. 2019) in Section 3. Further, we examine the existing population of hot Jupiters, studying existing trends in the mass–period distribution and discussing the contribution of TESS discoveries (Section 4). Our conclusions are summarized in Section 5.

2. Observations and Archival Data

We confirm and characterize TOI-558 and TOI-559 as planetary systems using TESS observations combined with ground-based photometric and spectroscopic follow-up observations from the TESS Follow-up Observing Program (TFOP) working group. Table 1 provides a list of the literature identifiers, magnitudes, and kinematics for TOI-558 and TOI-599.

[34] exoplanetarchive.ipac.caltech.edu/

Table 1
Literature and Measured Properties for TOI-558 and TOI-559

Other Identifiers				
		TOI-558	TOI-559	
		TIC 207110080	TIC 209459275	
		TYC 8497-00028-1	TYC 7019-00191-1	
	TESS Sector	2,3,29,30	4, 31	
Parameter	Description	Value	Value	Source
α_{J2000}	R.A. (R.A.)	02:49:09.9601	03:07:16.4958	1
δ_{J2000}	decl. (decl.)	−58:01:28.9180	−31:09:45.7019	1
B_T	Tycho B_T mag.	12.049 ± 0.126	11.792 ± 0.054	2
V_T	Tycho V_T mag.	11.309 ± 0.093	11.158 ± 0.052	2
G	Gaia *G* mag.	11.33 ± 0.02	10.98 ± 0.02	1
B_P	Gaia B_P mag.	11.58 ± 0.02	11.30 ± 0.02	1
R_P	Gaia R_P mag.	11.576 ± 0.02	10.52 ± 0.02	1
T	TESS mag.	10.988 ± 0.019	10.535 ± 0.018	3
J	2MASS J mag.	10.581 ± 0.03	9.985 ± 0.023	4
H	2MASS H mag.	10.309 ± 0.03	9.719 ± 0.022	4
K_S	2MASS K_S mag.	10.262 ± 0.02	9.638 ± 0.024	4
WISE1	*WISE1* mag.	10.216 ± 0.03	9.61 ± 0.03	5
WISE2	*WISE2* mag.	10.248 ± 0.03	9.65 ± 0.03	5
WISE3	*WISE3* mag.	10.236 ± 0.051	9.61 ± 0.035	5
WISE4	*WISE4* mag.	···	9.33 ± 0.49	5
μ_α	Gaia DR2 proper motion in R.A. (mas yr^{-1})	1.071 ± 0.042	-23.136 ± 0.031	1
μ_δ	Gaia DR2 proper motion in decl. (mas yr^{-1})	3.859 ± 0.042	-69.698 ± 0.040	1
π[a]	Gaia Parallax(mas)	2.4850 ± 0.033[a]	4.288 ± 0.037	1
$v \sin i_\star$	Rotational velocity (km s^{-1})	7.8 ± 0.5	4.08 ± 0.5	Sections 2.3 and 2.5
v_{mac}	macroturbulent broadening (km s^{-1})	5.9 ± 0.5	4.38 ± 0.5	Sections 2.3 and 2.5
U[b]	Space Velocity (km s^{-1})	3.8 ± 0.1	86.0 ± 0.7	Section 2.7
V	Space Velocity (km s^{-1})	-3.0 ± 0.3	-14.5 ± 0.3	Section 2.7
W	Space Velocity (km s^{-1})	-20.2 ± 0.4	4.7 ± 0.5	Section 2.7

Notes. The uncertainties of the photometry have a systematic error floor applied.
[a] Values have been corrected for the 30 μas offset as reported by Lindegren et al. (2018).
[b] *U* is in the direction of the Galactic center.
Sources are: (1) Gaia Collaboration et al. (2018), (2) Høg et al. (2000), (3) Stassun et al. (2018), (4) Cutri et al. (2003), (5) Cutri et al. (2012).

2.1. TESS Photometry

In the two-year primary mission, TESS completed 26 observation sectors, each of approximate length ∼27 days, covering the southern hemisphere in the first year-long cycle and the northern hemisphere in the second (Ricker et al. 2015). TESS recently began its first extended mission with a similar observation footprint that will cover over 90% of the sky in total, including a large part of the ecliptic plane. As of UT 2021 January 1, TESS has yielded 91 confirmed planets and 2440 planet candidates (including planets discovered prior to TESS), or TESS Objects of Interest (TOIs).[35]

TESS used four wide-field cameras, each with an f/1.4 aperture, 21″ pixel scale, and field of view of 24° × 24°, comprising a total field of view of 24° × 96° for each observing sector. TESS observations come with a cadence of 20 s, 2 minutes, or 30 minute full-frame images (FFIs; though we note the extended mission is now 10 minutes). The 20 s and 2 minute cadence targets are pre-selected before the sector is observed. Unfortunately, neither TOI-558 nor TOI-559 were pre-selected for short-cadence observations during the prime mission (later re-observed in 2 minute cadence during the extended mission; both were observed only in the FFIs, which cover the entire field of view at a 30 minute cadence.

TOI-558 (TIC 207110080) was observed by Camera 3 in both Sector 2, from UT 2018 August 22 to UT 2018 September 20, and Sector 3, from UT 2018 September 20 to UT 2018 October 18, during TESS's first year of the primary mission. TOI-559 (TIC 209459275) was observed by Camera 2 in Sector 4, from UT 2018 October 18 to UT 2018 November 15 (see Figure 1). We identified TOI-558 and TOI-559 as planet candidates through a search independent of the TESS planet search pipeline, using a standard box least-squares algorithm (Kovács et al. 2002) and visual examination of candidates from the MIT Quick Look Pipeline (QLP, Huang et al. 2020, and both candidates were designated as pre-selected targets for Cycle 3. TOI-558 was then re-observed by TESS again during Cycle 3, the first year of the extended mission, in Sector 29 (UT 2020 August 26 to UT 2020 September 22) and Sector 30 (UT 2020 September 22 to UT 2020 October 21) at a cadence of 2 minutes. TOI-559 was re-observed during Sector 31 from UT 2020 October 21 to UT 2020 November 19. The 2 minute

[35] https://tev.mit.edu/data/collection/193/

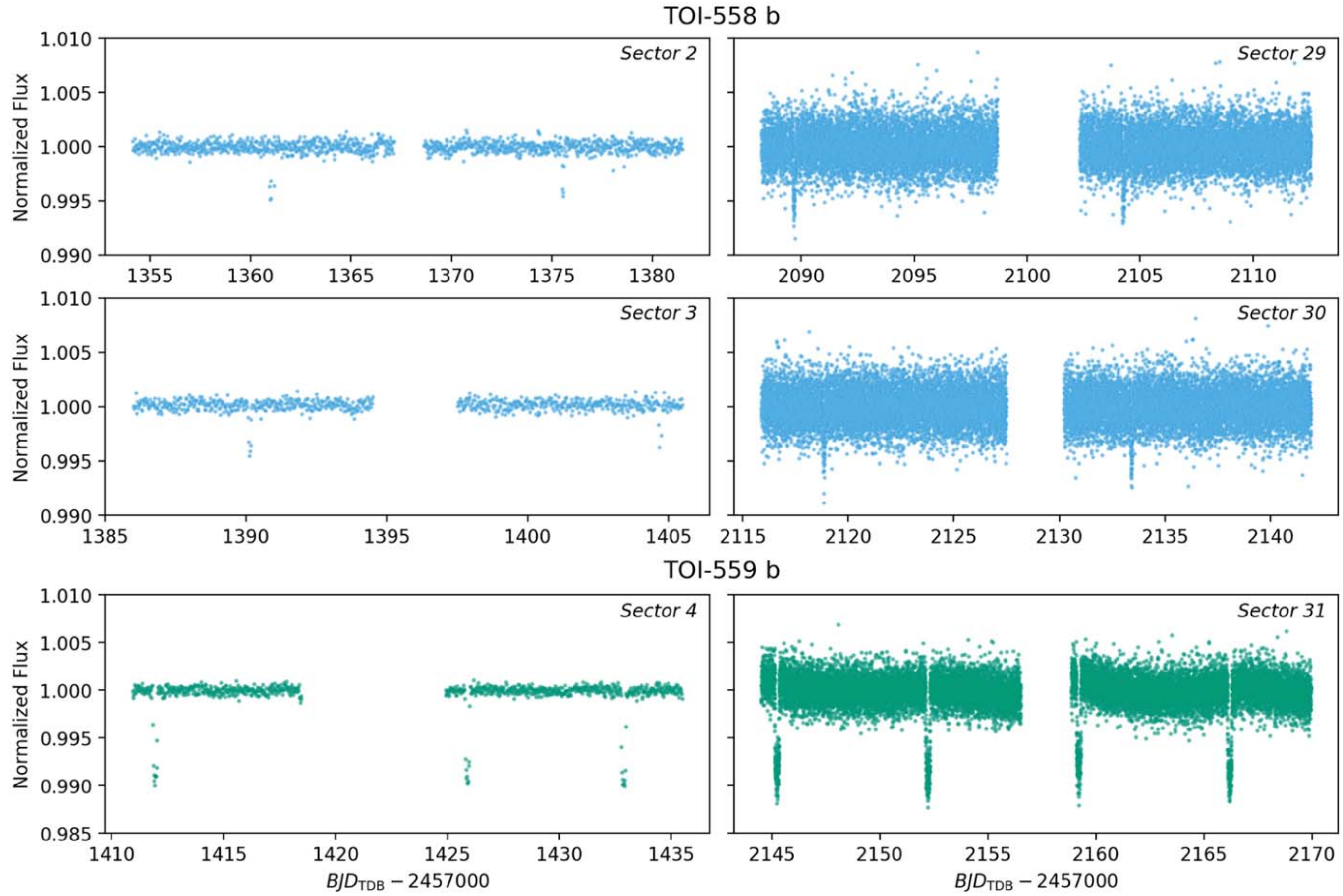

Figure 1. The full corrected light curves from TESS. The discovery light curves (left) extracted from the full-frame images are at a 30 minute cadence, from Sectors 2 and 3 for TOI-558 and Sector 4 for TOI-559, corrected using the quaternions following the description in Section 2.1. The additional light curves (right) extracted by the SPOC pipeline are at 2 minute cadence from Sectors 29–31 of the first extended mission (see Section 2.1), corrected with the PDC module. These are not the flattened light curves used for the global fitting.

observations were inspected by the Science Processing Operations Center (SPOC) team and did not indicate a false positive transit detection (Twicken et al. 2018; Li et al. 2019).

We extracted and processed light curves from the FFIs using `Tesscut` and the `Lightkurve` package for Python (Lightkurve Collaboration et al. 2018; Brasseur et al. 2019). The TESS SPOC (Jenkins et al. 2016) at NASA Ames Research Center processed the raw FFIs through a pipeline that calibrated the pixels and mapped world coordinate system information for each image frame. Our selected apertures included pixels with a mean flux of 80th percentile or greater within a 3 pixel radius of the target's center. We subtracted background-scattered light and deblended contamination from nearby stars using a simple target star model. We removed spacecraft systematic effects by decorrelating against the scattered background light and the standard deviation of the quaternion time series following Vanderburg et al. (2019). We performed the decorrelation using `Lightkurve`'s `RegressionCorrector` utility. We used the spline-fitting routine Keplerspline[36] (Vanderburg & Johnson 2014; Shallue & Vanderburg 2018) on these light curves to remove any remaining stellar variability, resulting in a flattened light curve. For TOI-559, the baseline fluxes observed during the two orbits of the TESS spacecraft in Sector 4 had a significant offset, so we detrended the two orbits separately. We omitted from further consideration all of the data obtained long before or after a transit, leaving roughly one full transit duration prior to each ingress and after each egress (including the full transit). These light curves were then used for the global modeling described in Section 3.

The 2 minute cadence TESS light curves for TOI-558 (from Sectors 29 and 30) and TOI-559 (from Sector 31) were extracted by the SPOC pipeline, based at the NASA Ames Research Center (Jenkins et al. 2016). Specifically, the data were downloaded, reduced, and analyzed by the SPOC pipeline, which included pixel-level calibrations, optimization of photometric aperture, estimation of the total flux contamination from other nearby stars, and extraction of the light curve. To remove systematic effects and instrumental artifacts, the Presearch Data Conditioning (PDC; Smith et al. 2012; Stumpe et al. 2014) module was applied to the extracted SPOC light curve. The resulting processed light curve was run through the SPOC Transiting Planet Search (TPS; Jenkins 2002) to identify any known or additional planet candidates. To remove any remaining low-frequency out-of-transit astrophysical or instrumental variability in the light curves, we use Keplerspline. We simultaneously fit the spline with a transit model to ensure that the transits were not distorted by the removal of low-frequency variability (see Vanderburg et al. 2016 and Pepper et al. 2020).

[36] https://github.com/avanderburg/keplersplinev2

Table 2
Ground-based Photometry Observations from TFOP for TOI-558 and TOI-559 Used in the Global Analysis

Date (UT)	Facility	Size (m)	Filter	FOV	Pixel Scale	Exp (s)	Additive Detrending
TOI-558							
2019 Sep 28	LCO SAAO	1 m	Sloan z'	$27' \times 27'$	0.″39	55	airmass, Width T1
2019 Oct 26	LCO CTIO	1 m	B	$27' \times 27'$	0.″39	34	airmass
2020 Nov 09	LCO CTIO	1 m	i	$27' \times 27'$	0.″39	25	airmass
TOI-559							
2019 Sep 27	PEST	0.3048	Rc	$27' \times 27'$	1.″2	60	None
2019 Oct 18	LCO SSO	1 m	Sloan z'	$27' \times 27'$	0.″39	35	airmass
2020 Aug 20	LCO SSO	1 m	Sloan i'	$27' \times 27'$	0.″39	25	none
2020 Aug 27	LCO SSO	1 m	Sloan i'	$27' \times 27'$	0.″39	25	airmass, sky/pixel T1

Note. See Section D in the appendix of Collins et al. (2017) for a description of each detrending parameter.

2.2. Ground-based Photometry from the TESS *Follow-up Observing Program Working Group*

To rule out any astrophysical false positives or systematic effects causing the transit events and to refine the timing and transit parameters, we obtained photometric transit follow up from ground-based telescopes. The TESS Follow-up Observing Program (TFOP)[37] Sub Group 1 (SG1), which specializes in ground-based time-series photometry, observed transits of both TOI-558 and TOI-559 with the Las Cumbres Observatory Global Telescope (LCOGT) network of 1 m telescopes[38] (Brown et al. 2013) and the Perth Exoplanet Survey Telescope (PEST).[39] The observations were scheduled using the `TAPIR` software package (Jensen 2013) and all observations but the ones taken by PEST were reduced and light curves were extracted using `AstroImageJ` (Collins et al. 2017). PEST uses a custom software suite to reduce the images and extract light curves, the `PEST Pipeline`.[40] These transit observations and facilities are listed in Table 2 and Figure 2. These observations not only extended the baseline, but also provided an independent check on the depth and duration of the transit as compared to what was observed by TESS.

2.3. PFS Spectroscopy (TOI-558)

TOI-558 was observed using the Planet Finder Spectrograph (PFS) on the 6.5 m Magellan Clay Telescope at Las Campanas Observatory in Chile (Crane et al. 2006, 2008, 2010), which has been extensively used to follow up and confirm TOIs (e.g., Teske et al. 2021). We obtained 14 radial velocity (RV) measurements from UT 2019 January 19 to UT 2019 February 18, which are shown in Table 3 and Figure 3. PFS is a high-resolution, optical (391–734 nm) spectrograph that utilizes an iodine cell to achieve highly precise RV (<2 m s^{-1}) observations. The PFS spectra were reduced and RVs were extracted using a custom IDL pipeline (Butler et al. 1996). These observations were taken with the new $10k \times 10k$ CCD, with a 0.″3 slit and at 3×3 binning with a resolving power of ($R \sim$110,000). While PFS can achieve sub-1 m s^{-1} precision, we chose shorter exposures with a typical RV precision of $\sim$5 m s^{-1} since our targets have very large RV semi-amplitudes ($>$30 m s^{-1}).

We derived stellar parameters, specifically the host star's metallicity, for TOI-558 from the iodine-free template spectrum obtained with PFS. The spectrum, in the region of 5000–5500 Å, was analyzed with the ZASPE package (Brahm et al. 2017), which performs a model comparison between the observed spectrum and a grid of the PHOENIX stellar atmosphere's synthetic spectra (Husser et al. 2013). ZASPE weights spectral regions based on their pre-determined importance to the stellar parameter determination and varies the depths of those spectral regions with a Monte Carlo analysis to determine the uncertainties and covariance of the derived stellar parameters. The resulting best-fit metallicity was $[\mathrm{Fe/H}] = -0.020 \pm 0.066$ dex, which we use as a prior on the global fit (see Section 3). Using the PFS template, we measured the $v \sin i_\star$ and macroturbulent broadening for TOI-558 following the methodology in Zhou et al. (2018). We measured $v \sin i_\star$ for TOI-558 to be be 4.1 ± 0.5 km s^{-1} and v_{mac} to be 4.4 ± 0.5 km s^{-1}.

2.4. TRES Spectroscopy (TOI-559)

Reconnaissance spectroscopic follow-up observations of TOI-559 were taken on three separate epochs at a resolving power of R $\sim$44,000 using the 1.5 m Tillinghast Reflector Echelle Spectrograph (TRES; Fűrész 2008).[41] TRES is located at the the Fred L. Whipple Observatory (FLWO) on Mt. Hopkins, AZ. The reduction and RV extraction pipeline details are described in Buchhave et al. (2010) and Quinn et al. (2012). With only three observations, we do not include these RVs in the global analysis (see Section 3). Nevertheless the extracted RVs yielded a semi-amplitude consistent with the global analysis. The TRES spectra were also used as an independent check on the metallicity from CHIRON. Using the Stellar Parameter Classification package (Buchhave et al. 2012), we derive a metallicity for TOI-559 of $[\mathrm{Fe/H}] = -0.24 \pm 0.08$ dex, consistent with what was found using CHIRON. Additionally, the TRES absolute velocity for TOI-559 was -14.03 ± 0.42 km s^{-1}, consistent with the Gaia DR2 results.

2.5. CHIRON Spectroscopy (TOI-559)

TOI-559 was observed with the CTIO High-Resolution spectrometer (CHIRON) on the CTIO 1.5 m telescope (Tokovinin et al. 2013). CHIRON covers a wavelength range of 420–880 nm, with a resolving power of 80,000. The RV measurements were extracted from the CHIRON spectra using a least-squares deconvolution technique described in Donati et al. (1997) and Zhou et al. (2021); the 22 RVs were taken between UT 2019 January 27 and UT 2019 September 20 and

[37] https://tess.mit.edu/followup/
[38] https://lco.global/observatory/telescopes/1-m/
[39] http://pestobservatory.com
[40] http://pestobservatory.com/the-pest-pipeline/
[41] http://www.sao.arizona.edu/html/FLWO/60/TRES/GABORthesis.pdf

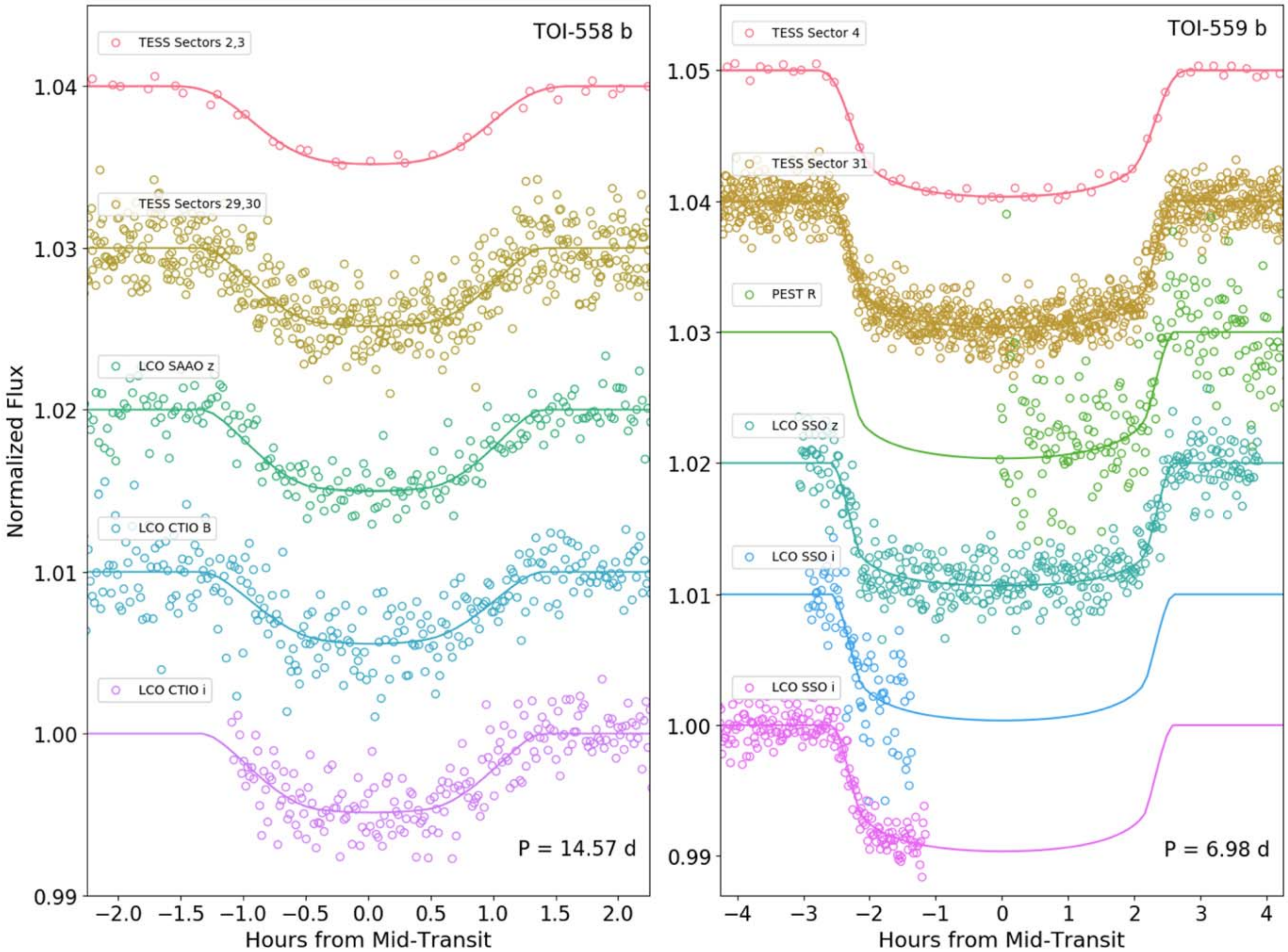

Figure 2. The phase-folded and detrended transit light curves for (left) TOI-558 and (right) TOI-559 from TESS and the TFOP working group. The solid colored lines correspond to the best-fit model from our global fit (see Section 3).

(The data used to create this figure are available.)

are shown in Table 3 and Figure 3. We check that the line-broadening velocity is not correlated with the measured radial velocities. We also note that both TOI 558 and 559 are slowly rotating stars, with rotational broadening velocities of 8 $\mathrm{km\,s^{-1}}$ and 4 $\mathrm{km\,s^{-1}}$, respectively. For stellar activity to affect our velocities at the 200 $\mathrm{m\ s^{-1}}$ level, as is our detected Doppler orbit, the stars should exhibit significant photometric modulation at the >2% level. We do not see any large stellar activity signatures in the TESS light curves, consistent with our interpretation that these target stars are quiet at the level suitable for our detections of their Doppler orbits.

We also use the CHIRON spectra to determine some constraints on the host star's metallicity and $v \sin i_\star$. The spectra were matched against an interpolated grid of ∼10,0000 observed spectra from the TRES database, previously classified using the Spectral Classification Pipeline (Buchhave et al. 2012). This library is interpolated using a gradient boost classifier algorithm in the *scikit-learn* machine-learning package. The CHIRON observed spectrum is then convolved against a Gaussian profile such that it matches the spectral resolution of observations in this library ($R = 44{,}000$). We measure the metallicity of TOI-559 to be $[\mathrm{Fe/H}] = -0.22 \pm 0.11$ dex, the effective temperature to be $T_{\mathrm{eff}} = 5784 \pm 50$ K, and the surface gravity to be $\log g = 4.18 \pm 0.10$ (cgs). We only use the metallicity as a Gaussian prior in the global fit, allowing the fit to constrain the host star's effective temperature and surface gravity using the spectral energy distribution and transit shape, respectively (see Section 3). We also derive the $v \sin i_\star$ for TOI-559 to be 7.8 ± 0.5 $\mathrm{km\,s^{-1}}$ and v_{mac} to be 5.9 ± 0.5 $\mathrm{km\,s^{-1}}$ following Zhou et al. (2018).

2.6. High-resolution Speckle Imaging

It is difficult to rule out the possibility of blended companion stars using TESS data alone given the size of the pixels. Contamination from blended stars can cause a false positive transit signal on the planetary candidate host star or affect the derived planetary radius (Ciardi et al. 2015; Ziegler et al. 2018). To check for very nearby stars not resolved by seeing-limited images and Gaia and account for any blends that would be included in the spectra, we obtained high-resolution speckle imaging of TOI-558 and TOI-559 from the Southern Astrophysical Research Telescope (SOAR; Tokovinin 2018). TOI-558 and TOI-559 were both observed on UT 2019 February 18 and had a sensitivity of $\Delta\mathrm{Mag} = 6.7$ and 7.2 at 1″, respectively. Figure 4 displays the reconstructed images as well as the limiting magnitude difference versus on-sky distance from the center of the target star. We see no signs of any nearby close (within 3″) companions in the SOAR observations of TOI-558 or TOI-559. For a detailed description of the observing strategy for TESS targets see Ziegler et al. (2020).

Using the Zorro instrument mounted on the 8 m Gemini South telescope on Cerro Pachon in Chile, we observed TOI-558 on UT 2020 December 23 and 29. The first observation had poor seeing, so we show the December 29th observation in Figure 4. TOI-559 was observed using the 'Alopeke instrument on UT 2019 October 09. 'Alopeke simultaneously observes in blue ($\frac{\lambda}{\Delta\lambda} = 562/54$ nm) and red ($\frac{\lambda}{\Delta\lambda} = 832/40$ nm) band passes, with inner working angles of 0.″026 for the blue and 0.″017 for the red. The instrument has a pixel scale of 0.″01. Three thousand 0.06 s images were obtained and combined for each star, and the Fourier analysis described in Howell et al. (2011) was performed on the combined image. The 'Alopeke observations confirm and extend to smaller inner working angles the results seen by SOAR, in that TOI-559 is a single star with no signs of any previously unknown companions to within the 5σ contrast limits obtained (see Figure 4). The observations had a sensitivity of Δmag = 5.557 for the blue and 7.375 for the red, at 1″ for TOI-559 and Δmag = 4.355 and 6.394 for TOI-558. The observations and full contrast curves can be found on https://exofop.ipac.caltech.edu/tess/.

2.7. Galactic Locations, Kinematics, Orbits, and Populations

We used the parallaxes, proper motions, radial velocities, and associated uncertainties of TOI-558 and TOI-559 from the Gaia DR2 catalog (Gaia Collaboration et al. 2018) to determine the location, kinematics, orbits, and associations of each system with known stellar populations following the analysis methodology performed by Burt et al. (2020). We corrected the DR2 parallaxes and uncertainties following Lindegren et al. (2018). We then used these parallaxes to estimate the distances to the systems. These distances and their uncertainties were then used in combination with the DR2 proper motions and radial velocities to determine the heliocentric UVW velocities of the host stars. We determined the UVW velocities with respect to the local standard of rest (LSR) using the determination of the Sun's motion relative to the LSR by Cośkunoǧlu et al. (2011). We adopt a coordinate system such that positive U is toward the Galactic center. These UVW values are shown in Table 1.

For each system, we estimated its Z height relative to the Sun, and then corrected for the $Z_{\odot} \simeq 30$ pc offset of the Sun from the Galactic plane as determined by Bovy (2017) based on local giants. We use the UVW velocities (with respect to the LSR) to estimate the likelihood that the star belongs to thin disk, thick disk, halo, or Hercules stream, using the categorization criteria of Bensby et al. (2014). We use the Galactic orbits estimated by Mackereth & Bovy (2018), and report estimates of the orbital parameters (apogalacticon, perigalaciton, eccentricity, and maximum excursion perpendicular to the plane). We estimated the spectral type of each host star using their effective temperatures (as given in Table 4) and the relations of Pecaut & Mamajek (2013). We then compared the position and orbits of the two systems to the scale height h_Z of stars of similar spectral type as determined by Bovy (2017).

We also considered whether either of the systems belong to any of the known nearby young associations using the BANYAN Σ (Bayesian Analysis for Nearby Young AssociatioNs Σ) tool (Gagné et al. 2018). The BANYAN Σ estimator assigned both hosts to be "field" stars.

Table 3
Radial Velocities for TOI-558 and TOI-559

Target	BJD_{TDB}(days)	RV(m s^{-1})	σ_{RV}(m s^{-1})	Facility
TOI-558	2458502.57047	137.8	4.6	PFS
TOI-558	2458503.60715	151.3	4.4	PFS
TOI-558	2458504.61284	120.7	5.0	PFS
TOI-558	2458505.57474	37.0	5.2	PFS
TOI-558	2458506.56937	−93.4	4.6	PFS
TOI-558	2458507.57311	−270.0	5.0	PFS
TOI-558	2458508.56806	−368.9	4.7	PFS
TOI-558	2458509.56851	−317.2	6.2	PFS
TOI-558	2458526.58483	−115.2	5.1	PFS
TOI-558	2458527.53828	−54.8	6.8	PFS
TOI-558	2458528.53871	0.0	4.8	PFS
TOI-558	2458529.54633	59.0	5.4	PFS
TOI-558	2458531.61868	165.5	5.7	PFS
TOI-558	2458532.54853	152.1	5.2	PFS
TOI-559	2458510.54861	−15924.9	33.2	CHIRON
TOI-559	2458511.60839	−16208.5	21.6	CHIRON
TOI-559	2458512.54877	−16119.7	22.1	CHIRON
TOI-559	2458526.54291	−16162.9	17.0	CHIRON
TOI-559	2458527.57189	−15526.1	33.6	CHIRON
TOI-559	2458529.53872	−15143.5	28.0	CHIRON
TOI-559	2458531.55750	−16018.5	16.7	CHIRON
TOI-559	2458537.57692	−15573.6	13.7	CHIRON
TOI-559	2458539.57232	−16224.7	22.9	CHIRON
TOI-559	2458541.51279	−15590.0	16.4	CHIRON
TOI-559	2458542.51358	−15008.6	13.2	CHIRON
TOI-559	2458543.51021	−15169.4	23.8	CHIRON
TOI-559	2458550.51777	−15165.0	25.0	CHIRON
TOI-559	2458551.50301	−15612.5	25.4	CHIRON
TOI-559	2458552.51271	−15998.8	26.6	CHIRON
TOI-559	2458553.49918	−16231.8	28.1	CHIRON
TOI-559	2458554.49890	−16175.8	54.2	CHIRON
TOI-559	2458741.86403	−16340.3	21.7	CHIRON
TOI-559	2458742.79259	−16371.4	33.3	CHIRON
TOI-559	2458743.87250	−15812.6	23.1	CHIRON
TOI-559	2458744.81891	−15203.6	24.5	CHIRON
TOI-559	2458745.85030	−15210.3	30.6	CHIRON
TOI-559	2458746.84768	−15634.3	21.6	CHIRON
TOI-559	2458511.60506	−896.80	20.02	TRES
TOI-559	2458515.62512	218.75	20.29	TRES
TOI-559	2458738.98177	104.78	34.18	TRES

Note. The median absolute RV has been subtracted off the PFS and TRES RVs.

TOI-558 is at a distance of $d = 402 \pm 5$ pc from the Sun, consistent with the posterior value listed in Table 4. Its vertical distance from the Galactic plane is $Z + Z_{\odot} \simeq -291$ pc. It has Galactic velocities with respect to the LSR of $(U, V, W) = (3.8 \pm 0.1, -3.0 \pm 0.3, -20.2 \pm 0.4)$ km s^{-1}. According to the categorization of Bensby et al. (2014), the system has a ~98% probability of belonging to the thin disk. The Galactic orbit has a perigalacticon of $R_p = 7.04$ kpc, and apogalacticon of $R_a = 8.07$ kpc, an eccentricity of $e = 0.07$, and a maximum Z excursion from the Galactic plane of $Z_{\max} = 460$ pc. Thus, the orbit is consistent with the current location of the system. The scale height of stars of similar spectral type (F5.5V) is only 85 pc. Nevertheless, there is a non-negligible probability that a star belonging to this population can have a maximum excursion above the plane that is several scale heights.

TOI-559 is at distance of $d = 233 \pm 2$ pc from the Sun, consistent with the posterior value listed in Table 4. Its vertical

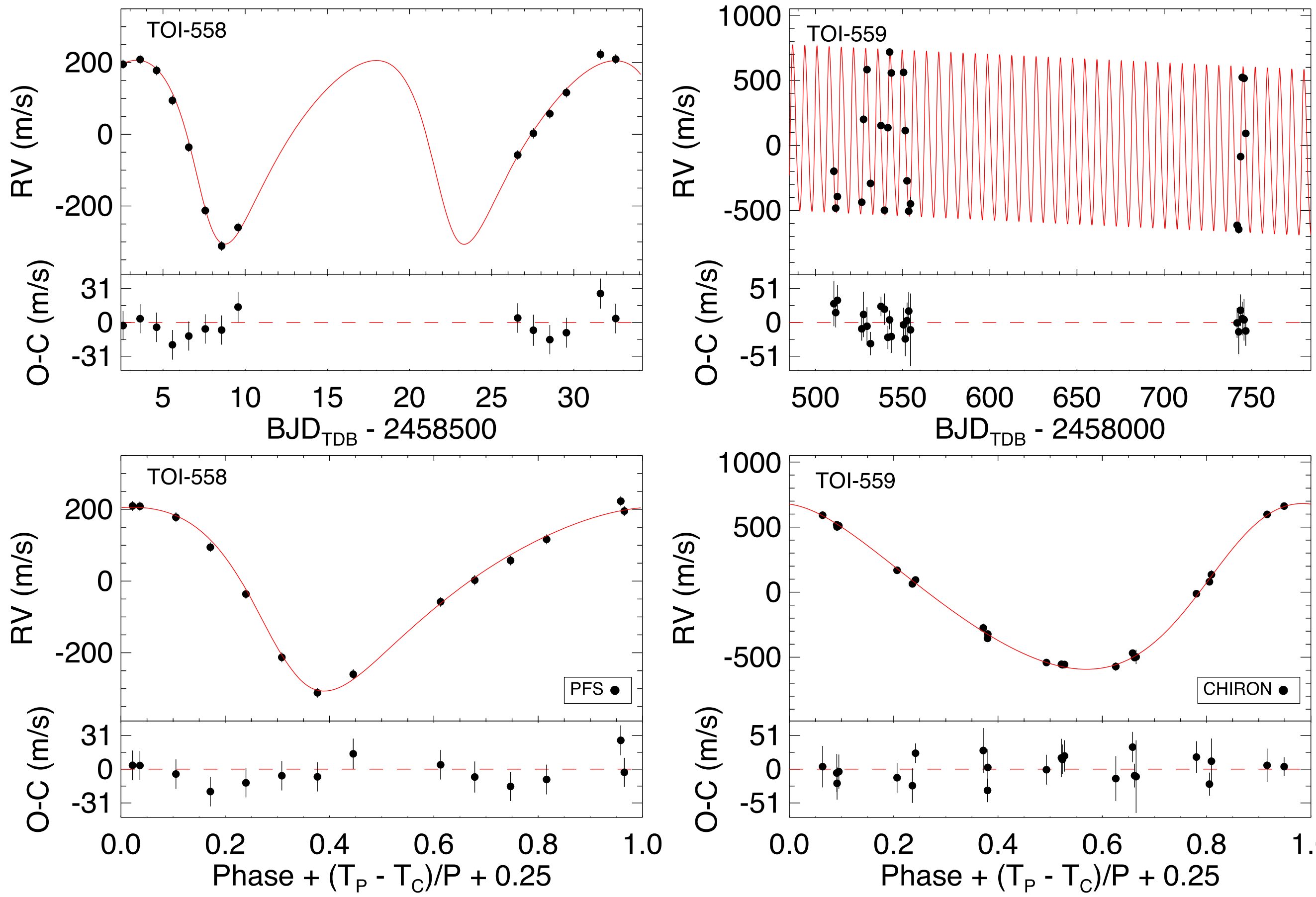

Figure 3. (Top) The radial velocity observations over time for (left) TOI-558 b from PFS and (right) TOI-559 b from CHIRON. The RVs phase-folded to the best-fit periods are shown above. The EXOFASTv2 model fit is shown in red.

distance from the Galactic plane is $Z + Z_\odot \simeq -172$ pc. It has Galactic velocities with respect to the LSR of (U, V, W) $= (86.0 \pm 0.7, \ -14.5 \pm 0.3, \ 4.7 \pm 0.5)$ kms^{-1}. According to the categorization of Bensby et al. (2014), the system has a ~92% probability of belonging to the thin disk, and an ~8% probability of belonging to the thick disk. The Galactic orbit has a perigalacticon of $R_p = 5.32$ kpc, and apogalacticon of $R_a = 10.3$ kpc, an eccentricity of $e = 0.022$, and a maximum Z excursion from the Galactic plane of $Z_{\max} = 320$ pc. Thus the orbit is consistent with the current location of the system and with the scale height of 108 pc for stars of similar spectral type (G0V). Although this system has a non-negligible probability of belonging to the thick disk, it is nevertheless more likely to be a member of the thin disk. We estimate an age of ~7 Gyr for this system from our global analysis Table 4, which may explain its relatively large value of the eccentricity and maximum vertical excursion above the plane of the orbit.

3. EXOFASTv2 Global Fit for TOI-558 and TOI-559

In order to characterize the planetary systems, we modeled the observations obtained in Section 2 with `EXOFASTv2`, a global fitting suite for exoplanets (Eastman et al. 2013, 2019) to simultaneously fit the TESS and TFOP SG1 photometry and the PFS and CHIRON RVs. `EXOFASTv2` uses a differential evolution Markov Chain Monte Carlo (MCMC) to simultaneously model the star and planet globally and self-consistently. For our fits of TOI-558 and TOI-559, we conducted a fit of the spectral energy distribution (SED) of the host star (see Table 1 for a list of the broadband photometric measurements used in the SED analysis) simultaneously with the available radial velocities and photometry. We imposed Gaussian priors on the Gaia parallaxes (Gaia Collaboration et al. 2018; accounting for the 30μ offset as reported by Lindegren et al. 2018) and the stellar metallicities obtained from spectroscopy ([Fe/H] $= -0.020 \pm 0.066$ for TOI-558, -0.22 ± 0.11 for TOI-559; see Sections 2.5 and 2.3), and an upper limit on the maximum line-of-sight extinction (0.06169 and 0.04154) according to Schlegel et al. (1998) and Schlafly & Finkbeiner (2011). With the addition of cataloged broadband photometry (see Table 1) and SED model constraints, the fit provides a precise constraint on the stellar radius ($R_\star$). Within the fit, `EXOFASTv2` placed a lower bound on the precision (~2%) of the bolometric flux ($F_{\rm bol}$) for the SED, which corresponds to the variations in $F_{\rm bol}$ from different calculation techniques (Zinn et al. 2019). `EXOFASTv2` uses the MESA Isochrones and Stellar Tracks (MIST) stellar evolution models (Paxton et al. 2011, 2013, 2015; Choi et al. 2016; Dotter 2016), thereby encoding the physics of stellar evolution, where the global model is penalized for large differences from MIST-predicted stellar values. We ran MCMC fits for both systems, with strict convergence criteria of a Gelman Rubin statistic of less than 1.01 and at least 1000 independent draws in each parameter. We also fit for a dilution term on the TESS observations. Specifically, we adopt a Gaussian prior on the contamination ratio equal to that reported by the TESS Input Catalog (TIC, Stassun et al. 2018), with a dispersion of 10%. This assumes

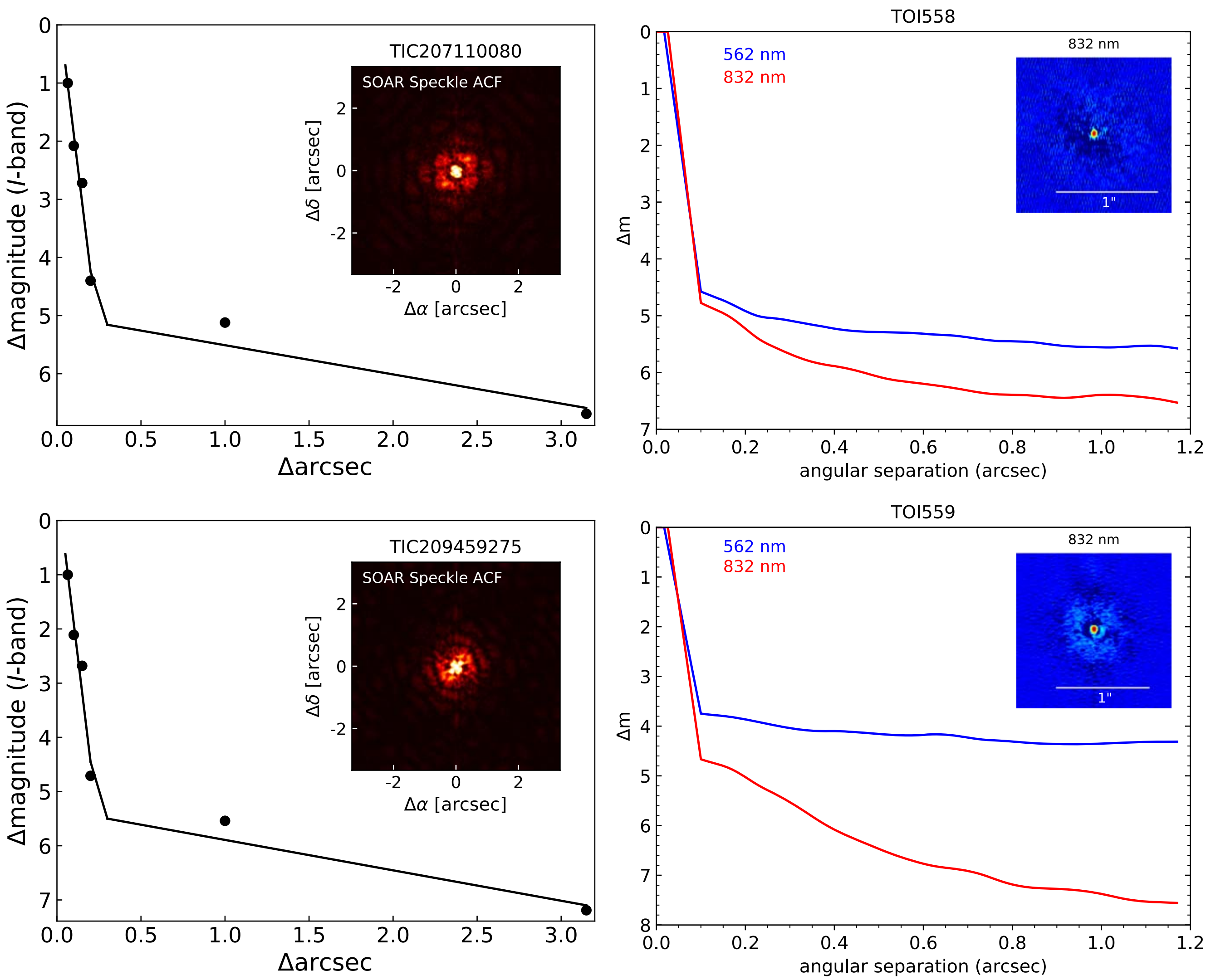

Figure 4. The (left) Speckle interferometric observations for TOI-558 and TOI-559 of the two targets from the Southern Astrophysical Research Telescope (SOAR). The autocorrelation function is shown inset the contrast curve from SOAR. The (right) Gemini South Zorro and Gemini North 'Alopeke speckle imaging 5σ contrast curves are shown along with the reconstructed images (embedded) of TOI-558 and TOI-559.

that the TESS light curves have been corrected for known companions in the aperture to better than 10%. Although we deblend the FFI light curve, the SPOC pipeline corrects the 2 minute light curve and no unknown companions were detected in our high-resolution imaging (see Section 2.6 and Figure 4). This provides an independent check on those corrections and properly propagate uncertainties. In both cases, the fitted dilution found by `EXOFASTv2` is consistent with zero. The TFOP SG1 photometry for each system was detrended within the full fit using an additive model and the detrending parameters seen in Table 1. See Collins et al. (2017), appendix D, for a description of each detrending parameter listed. The fitted transit data for TOI-558 and TOI-559 are shown in Figure 2, the RV fit is shown in Figure 3, and the resulting median values and 1σ uncertainties for all fitted stellar and planetary parameters are displayed in Tables 4 and 5. At the top of Table 4 is a list of the priors used in the fit. See Eastman et al. (2019) for a full list of the fitted and derived parameters from `EXOFASTv2` and any bounds on fitted parameters.

4. Discussion

Our global model shows that TOI-558 is an F-type star with a mass of $1.349^{+0.064}_{-0.065}$ $M_\odot$ and a radius of $1.496^{+0.042}_{-0.040}$ $R_\odot$. TOI-558 b is a 3.61 ± 0.15 $M_{\rm J}$ planet in a 14.57 days orbit with an eccentricity of $0.298^{+0.022}_{-0.020}$. We characterize TOI-559 as a G dwarf with a stellar mass of 1.026 ± 0.057 $M_\odot$ and radius $1.233^{+0.028}_{-0.026}$ $R_\odot$; TOI-559 b is $6.01^{+0.24}_{-0.23}$ $M_{\rm J}$ and its orbital period is 6.98 days with an eccentricity of $0.151^{+0.012}_{-0.011}$. Although both planets' masses are likely consistent with core accretion, the mass for TOI-559 b is near the theoretical lower limit for disk fragmentation (Moe & Kratter 2019).

We note that we detect a significant long-term RV trend in the multi-year radial velocities of TOI-559. The trend is well fit by a linear velocity variation at a rate of 0.65 m day^{-1}. Assuming a circularly bound orbit for the companion, such a trend would correspond to a substellar mass companion with a semimajor axis less than ∼8 au, or a stellar-mass companion farther out. Given the lack of a detected companion in our high-spatial-resolution observations, stellar companions with separations of >20 au are unlikely, as they would need to be of

Table 4
Median Values and 68% Confidence Interval of the Posterior Distribution for the Global Models

Priors:		TOI-558 b	TOI-559 b
Gaussian	π Gaia Parallax (mas)	2.53691 ± 0.04045	4.28820 ± 0.03673
Gaussian	[Fe/H] Metallicity (dex)	-0.02 ± 0.07	-0.22 ± 0.11
Upper Limit	A_V V-band extinction (mag)	0.0617	0.0415
Gaussian′	D_T Dilution in *Tess*	0.00000 ± 0.000317	0.00000 ± 0.000102
Parameter	Units	Values	
M[a]	Mass ($M_\odot$)	$1.349^{+0.064}_{-0.065}$	1.026 ± 0.057
R[a]	Radius ($R_\odot$)	$1.496^{+0.042}_{-0.040}$	$1.233^{+0.028}_{-0.026}$
L[c]	Luminosity ($L_\odot$)	$3.52^{+0.16}_{-0.14}$	$1.688^{+0.087}_{-0.069}$
$F_{\rm Bol}$	Bolometric Flux$\times 10^{-10}$ (cgs)	$6.99^{+0.26}_{-0.22}$	$9.92^{+0.49}_{-0.37}$
ρ_*	Density (g cm^{-3})	$0.568^{+0.054}_{-0.051}$	$0.774^{+0.053}_{-0.058}$
$\log g$	Surface gravity (cgs)	$4.218^{+0.030}_{-0.031}$	$4.268^{+0.024}_{-0.028}$
$T_{\rm eff}$	Effective Temperature (K)	6466^{+95}_{-93}	5925^{+85}_{-76}
[Fe/H]	Metallicity (dex)	$-0.004^{+0.059}_{-0.055}$	$-0.069^{+0.065}_{-0.079}$
$[{\rm Fe/H}]_0$	Initial Metallicity	$0.137^{+0.051}_{-0.049}$	$-0.001^{+0.063}_{-0.068}$
Age	Age (Gyr)	$1.79^{+0.91}_{-0.73}$	$6.8^{+2.5}_{-2.0}$
EEP[b]	Equal Evolutionary Phase	345^{+22}_{-14}	414^{+14}_{-19}
A_V	V-band extinction (mag)	$0.033^{+0.020}_{-0.022}$	$0.023^{+0.013}_{-0.015}$
σ_{SED}	SED photometry error scaling	$1.02^{+0.34}_{-0.22}$	$0.99^{+0.43}_{-0.25}$
ϖ	Parallax (mas)	2.491 ± 0.032	$4.289^{+0.036}_{-0.037}$
d	Distance (pc)	$401.4^{+5.3}_{-5.1}$	233.2 ± 2.0
$\dot{\gamma}$	RV slope (m/s/day)	…	$-0.650^{+0.064}_{-0.065}$
Planetary Parameters:			
P	Period (days)	14.574071 ± 0.000026	6.9839095 ± 0.0000051
R_P	Radius ($R_{\rm J}$)	$1.086^{+0.041}_{-0.038}$	$1.091^{+0.028}_{-0.025}$
M_P	Mass ($M_{\rm J}$)	3.61 ± 0.15	$6.01^{+0.24}_{-0.23}$
T_0[d]	Optimal conjunction Time (BJD$_{\rm TDB}$)	$2458871.07253 \pm 0.00053$	$2458893.81305 \pm 0.00023$
a	Semimajor axis (AU)	$0.1291^{+0.0020}_{-0.0021}$	0.0723 ± 0.0013
i	Inclination (Degrees)	$86.24^{+0.19}_{-0.22}$	$89.08^{+0.52}_{-0.38}$
e	Eccentricity	$0.298^{+0.022}_{-0.020}$	$0.151^{+0.012}_{-0.011}$
$\tau_{\rm circ}^{\pi}$	Tidal circularization timescale (Gyr)	347^{+100}_{-87}	$42.1^{+5.1}_{-5.6}$
ω_*	Argument of Periastron (Degrees)	$132.3^{+3.6}_{-3.8}$	$-62.3^{+3.0}_{-2.6}$
$T_{\rm eq}$	Equilibrium temperature (K)	1061^{+13}_{-12}	1180^{+18}_{-16}
K	RV semi-amplitude m s^{-1}	257.1 ± 6.5	$633.0^{+7.9}_{-8.4}$
R_P/R_*	Radius of planet in stellar radii	$0.0746^{+0.0013}_{-0.0011}$	$0.09097^{+0.00056}_{-0.00050}$
a/R_*	Semimajor axis in stellar radii	$18.56^{+0.57}_{-0.58}$	$12.61^{+0.28}_{-0.32}$
Depth	Flux decrement at mid transit	$0.00557^{+0.00019}_{-0.00017}$	$0.008276^{+0.00010}_{-0.000090}$
τ	Ingress/egress transit duration (days)	$0.0385^{+0.0045}_{-0.0034}$	$0.01884^{+0.0011}_{-0.00087}$
T_{14}	Total transit duration (days)	$0.1127^{+0.0020}_{-0.0019}$	$0.21459^{+0.0010}_{-0.00090}$
b	Transit Impact parameter	$0.9073^{+0.0066}_{-0.0067}$	$0.230^{+0.088}_{-0.13}$
$T_{S,14}$	Total eclipse duration (days)	0.00 ± 0.00	$0.1659^{+0.0045}_{-0.0043}$
ρ_P	Density (g cm^{-3})	$3.50^{+0.43}_{-0.41}$	$5.74^{+0.42}_{-0.46}$
$\log g_P$	Surface gravity	$1.16358088 \pm 0.00000078$	$0.84409860^{+0.00000031}_{-0.00000032}$
T_S	Time of eclipse (BJD$_{\rm TDB}$)	2458366.38 ± 0.15	$2458408.745^{+0.020}_{-0.021}$
$e\cos\omega_*$		-0.200 $\pm$ 0.016	$0.0700^{+0.0045}_{-0.0047}$
$e\sin\omega_*$		$0.221^{+0.024}_{-0.022}$	-0.133 $\pm$ 0.013
d/R_*	Separation at mid transit	$13.85^{+0.73}_{-0.75}$	$14.21^{+0.42}_{-0.44}$

Notes.
[a] The initial metallicity is the metallicity of the star when it was formed.
[b] The equal evolutionary point corresponds to static points in a star's evolutionary history when using the MIST isochrones and can be a proxy for age. See Section 2 in Dotter (2016) for a more detailed description of EEP.
[c] Optimal time of conjunction minimizes the covariance between T_C and period.
[d] The tidal quality factor (Q_S) is assumed to be 10^6 and is calculated using Equation (2) from Adams & Laughlin (2006). In our analysis, we assume the TESS correction for blending should be better than 10%. Therefore, we adopt a 10% prior on the blending determined from TICv8 (Stassun et al. 2018).

significant mass, and therefore luminosity, to induce our observed trend. TOI-559 is worthy of long-term RV monitoring to unveil the nature of its companion.

With high planetary masses and significant orbital eccentricities, TOI-558 b and TOI-559 b occupy a parameter space with few known planets. Only around two dozen previously

Table 5
Median Values and 68% Confidence Intervals for the Global Models

TOI-558							
Wavelength Parameters:		B	i‘	z‘	TESS		
u_1	linear limb-darkening coeff	$0.474^{+0.048}_{-0.047}$	0.206 ± 0.048	0.169 ± 0.046	$0.225^{+0.028}_{-0.029}$		
u_2	quadratic limb-darkening coeff	0.244 ± 0.048	0.306 ± 0.049	$0.310^{+0.047}_{-0.048}$	0.318 ± 0.028		
A_D	Dilution from neighboring stars	…	…	…	0.00000 ± 0.00032		
Telescope Parameters:		PFS					
$\gamma_{\rm rel}$	Relative RV Offset m s^{-1}	$-59.5^{+4.8}_{-4.6}$					
σ_J	RV Jitter m s^{-1}	$15.4^{+5.6}_{-3.8}$					
σ_J^2	RV Jitter Variance	240^{+200}_{-100}					
Transit Parameters:		TESS Sector 2	TESS Sector 3	TESS Sectors 29 + 30	LCOSAAO (z’) UT 2019-09-28	LCOCTIO (B) UT 2019-10-26	LCOCTIO (i’) UT 2020-11-06
σ^2	Added Variance	$0.000000001^{+0.000000056}_{-0.000000040}$	$0.000000126^{+0.000000091}_{-0.000000064}$	$-0.000000166^{+0.000000099}_{-0.000000095}$	$0.00000032^{+0.00000014}_{-0.00000012}$	$0.00000162^{+0.00000028}_{-0.00000025}$	$0.00000098^{+0.00000023}_{-0.00000020}$
F_0	Baseline flux	1.000105 ± 0.000077	$0.999951^{+0.000094}_{-0.000095}$	$1.000058^{+0.000046}_{-0.000047}$	$1.000034^{+0.000090}_{-0.000089}$	1.00031 ± 0.00012	1.00248 ± 0.00014
C_0	Additive detrending coeff	…	…	…	$0.00025^{+0.00025}_{-0.00024}$	-0.00410 $\pm$ 0.00027	$0.00151^{+0.00028}_{-0.00029}$
C_1	Additive detrending coeff	…	…	…	$0.00068^{+0.00022}_{-0.00021}$	…	…
TOI-559							
Wavelength Parameters:		R	i‘	z‘	TESS		
u_1	linear limb-darkening coeff	0.291 ± 0.049	0.269 ± 0.035	0.189 ± 0.040	$0.287^{+0.023}_{-0.024}$		
u_2	quadratic limb-darkening coeff	$0.273^{+0.048}_{-0.049}$	$0.290^{+0.035}_{-0.034}$	$0.269^{+0.045}_{-0.046}$	$0.284^{+0.028}_{-0.027}$		
A_D	Dilution from neighboring stars	…	…	…	0.00000 ± 0.00010		
Telescope Parameters:		CHIRON					
$\gamma_{\rm rel}$	Relative RV Offset[4] m s^{-1}	-15725.8 $\pm$ 6.3					
σ_J	RV Jitter m s^{-1}	$13.6^{+7.6}_{-8.2}$					
σ_J^2	RV Jitter Variance	180^{+270}_{-150}					
Transit Parameters:		Sector 4 01	Sector 4 O2	Sector 31			
σ^2	Added Variance	$0.000000030^{+0.000000034}_{-0.000000026}$	$0.000000003^{+0.000000018}_{-0.000000015}$	$0.000000006^{+0.000000052}_{-0.000000050}$			
F_0	Baseline flux	$1.000008^{+0.000055}_{-0.000054}$	1.000008 ± 0.000035	$1.000033^{+0.000029}_{-0.000030}$			
		PEST UT 2019-09-27 (R)	LCOSSO UT 2019-10-18 (z’)	LCOSSO UT 2020-08-20 (i’)	LCOSSO UT 2020-08-27 (i’)		
σ^2	Added Variance	$0.00000727^{+0.00000097}_{-0.00000086}$	$0.00000066^{+0.00000020}_{-0.00000019}$	$0.0000064^{+0.0000013}_{-0.0000011}$	$0.00000069^{+0.00000014}_{-0.00000012}$		
F_0	Baseline flux	1.00291 ± 0.00019	1.000015 ± 0.000095	1.00007 ± 0.00031	$0.999998^{+0.000083}_{-0.000082}$		
C_0	Additive detrending coeff –	$-0.00054^{+0.00029}_{-0.00028}$	…	$-0.00031^{+0.00022}_{-0.00021}$			
C_1	Additive detrending coeff	…	…	$0.00008^{+0.00058}_{-0.00057}$			

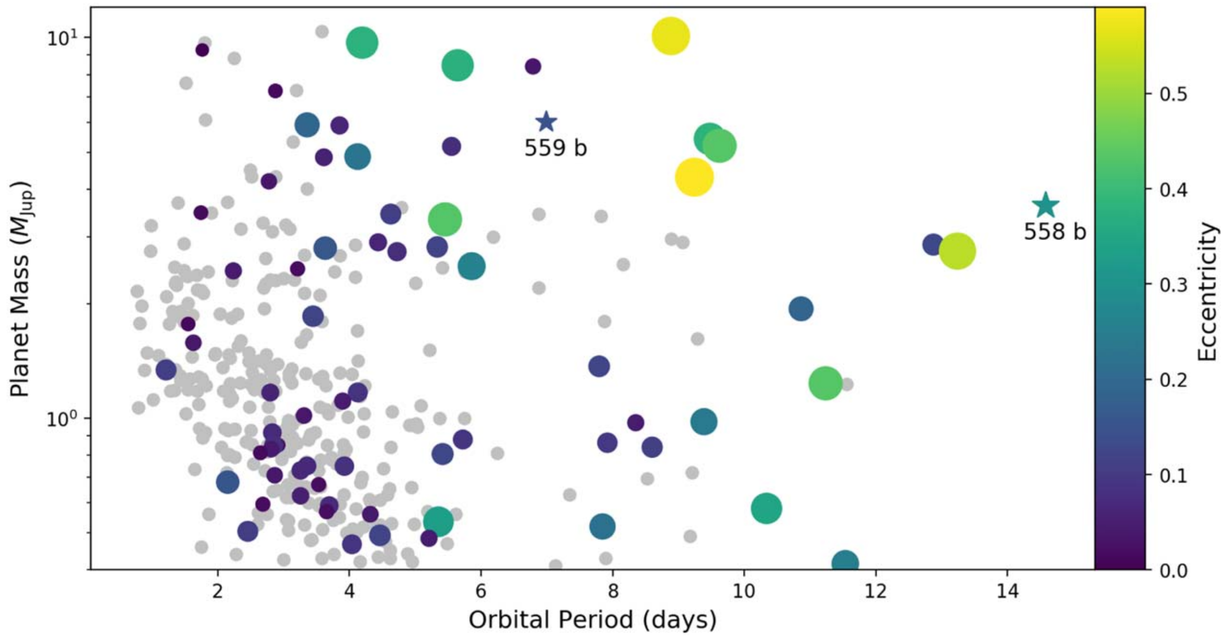

Figure 5. The population of transiting giant planets with periods less than 15 days and mass >0.4 $M_{\rm J}$, shown as a function of orbital period versus planet mass, as of UT 2020 November 1. Color and size indicate 1σ detection of orbital eccentricity; planets shown in gray do not have significant eccentricity.

confirmed transiting giant planets with periods between 5 and 15 days show eccentricity that differs from zero by more than 1 sigma (see Figure 5).[42] Most ground-based surveys have had poor completeness for planets with periods longer than 5 days (Gaudi et al. 2005), though TESS, which has near-complete sensitivity to hot Jupiters across the main-sequence (Zhou et al. 2019), will yield many more discoveries in this parameter space. In addition to being particularly massive, TOI-558 b and TOI-559 b have relatively high orbital eccentricities (0.3 and 0.15), indicating that these planets may have migrated to their current orbits through dynamical interactions. Based on the ages of the host stars and our estimates of their respective tidal circularization timescales (see Table 4[π]), we expect that neither of these systems has had sufficient time to circularize.

4.1. Period–Mass Distribution

Like eccentricity, the masses of hot Jupiters may provide clues to their evolutionary processes. For example, if hot Jupiters form in situ then it is predicted that there may be a $a \sim M_P^{-2/7}$ relationship that can be observed in the distribution of planet parameters (Bailey & Batygin 2018). The known population of transiting giant planets with reported masses greater than 0.4 Jupiter masses and orbital periods <15 days is shown in Figure 5 (we exclude planets that do not have reported uncertainties on the mass in the NASA Exoplanet Archive). With TESS expected to eventually be magnitude-limited for all transiting hot Jupiters ($P < 10$ days), we can test whether possible trends may already exist in the mass distribution of hot Jupiters (Rodriguez et al. 2019b). To probe this question, we include TOI-558 b and TOI-559 b in a study of the known population of hot Jupiters with periods shorter than 10 days, evaluating the potential existence of multiple populations. We use the *Scipy* implementations of the two-sample Kolmogorov–Smirnov (K–S) test (Massey 1951; Grover 1977) and a two-sample Anderson–Darling (A–D) test (Scholz & Stephens 1987) to qualitatively identify possible splits in the total population. Across a range of orbital period values, we divide the population into two samples, one with periods shorter than the given value and one with periods longer, and apply the K–S and A–D tests to those two distributions. As shown in Figures 6 and 7, we find a minimum p-value when the population split occurs between 5 and 5.5 days, at roughly 5.2 days with the K–S test and 5.4 days with the A–D test. In order to limit the influence of detection bias against lower-mass giant planets at longer periods, we include only transiting planets and only those with masses greater than 0.4 $M_{\rm J}$ (with reported mass uncertainties). Given the presence of detection biases at long periods and low masses, it is possible that our sample selection criteria ($M_p > 0.4\,M_{\rm J}$) could affect the result. We therefore rerun the test using 0.3 and 0.5 $M_{\rm J}$ for the minimum mass cutoff for the sample, but we find no qualitative change in the location of the minimum p-value. The presence of this p-value valley may suggest that there are two distributions separated near 5.2 days drawn from distinct parent distributions. The short-period (with 311 planets) and long-period (with 42 planets) samples have mean masses and standard errors of approximately 1.59 ± 0.09 $M_{\rm J}$ and 2.31 ± 0.32 $M_{\rm J}$, respectively. The mass distributions and cumulative mass distributions of the two samples are shown in Figure 7.

We caution that the current population of hot giant planets is a heterogeneous sample that comes from a variety of surveys. There are a number of possible biases in the present sample. For example, ground-based surveys have yielded fewer discoveries at longer periods, and there may also be a detection bias against the lowest masses among them. Physical factors, including the effect of tidal evolution on short-period planets (Jackson et al. 2009), influence the primordial mass–period distribution. Specifically, these physical factors result in observed features in the population, like the Neptune desert that may extend out to 10 days but is clearly deficient in planets inside of ~2.5 days (see Figure 7). Even for an unbiased

[42] as of UT 2020 November 1, https://exoplanetarchive.ipac.caltech.edu/.

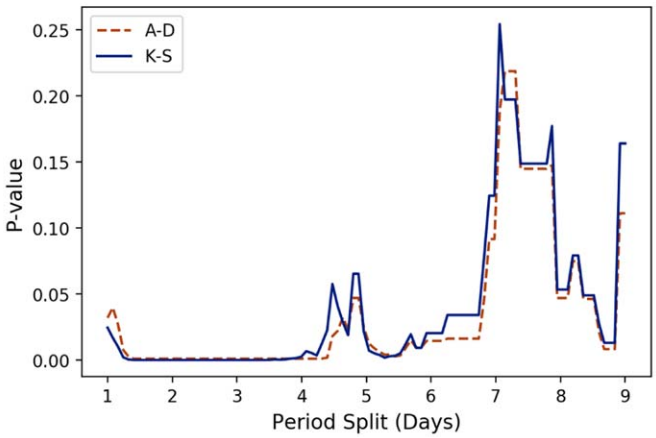

Figure 6. The two-sample Kolmogorov–Smirnov (K–S) and Anderson–Darling (A–D) tests applied to the short-period ($P < 10$ days) giant planet ($M_p > 0.4\ M_J$) population split at orbital periods ranging from 1 to 9 days. The *x*-axis is the period at which the population is split into two samples, and the *y*-axis is the resulting *p*-value. Tidal forces influence the distribution at short periods, possibly shaping the broad minimum between ∼1.5 and 4 days, while the minimum at ∼9 days is likely due to the small sample size at longer periods. The remaining minimum at ∼5.3 days has no obvious explanation, not showing significant dependence on the lower mass limit chosen for the sample, and could indicate a true break between two distributions.

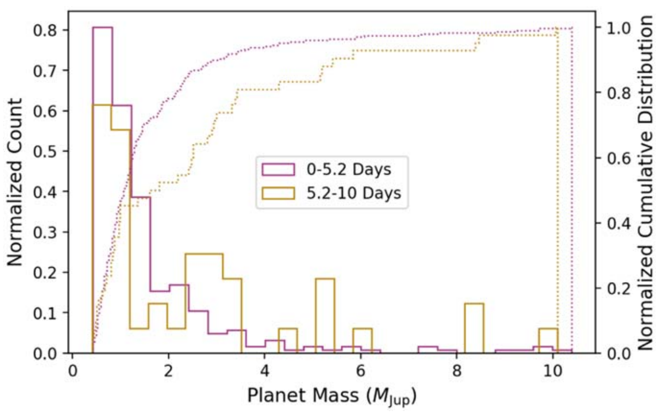

Figure 7. The mass distributions (solid) and cumulative mass distributions (dashed) of all known hot Jupiters with measured masses >0.4 M_J, split at the position of the K–S *p*-value valley from Figure 6 ($P \approx 5.2$ days) into two samples. We include 311 planets with periods less than ∼5.2 days and 42 with periods between ∼5.2 and 10 days.

sample, it is also possible that an apparent minimum in the *p*-value like the one we observe could be equally well described by a single, continuous model (e.g., Schlaufman 2015). Future investigation is warranted, as a more careful characterization of the population may provide constraints on hot Jupiter formation channels. The presence (and characteristics) of two separate hot Jupiter populations—or a single, continuous relationship—in the mass–period plane could be compared to model predictions and simulations of different formation processes and migration mechanisms. There are many confounding variables to consider, such as host-star properties, metallicity, system architectures, likely disk conditions, and more, all of which may affect planetary properties and the efficiency of migration mechanisms, and in turn, the expected resulting mass–period distribution. Simply identifying the broad characteristics of the population in mass–period space will require additional discoveries, so a large ensemble—like the complete transiting sample from TESS—will likely be required to draw firm conclusions. TOI-558 b and TOI-559 b represent two examples of planets that can contribute to these types of investigations.

5. Conclusion

We present the discovery and detailed characterization of two short-period massive giant planets from the TESS FFIs. Globally modeling photometric and spectroscopic observations from TESS and ground-based facilities using EXOFASTv2, we confirm TOI-558 b as a 3.62 ± 0.15 M_J planet in a 14.574076 ± 0.000025 day orbit around an F-type star, and TOI-559 b to be a $6.01^{+0.24}_{-0.23}$ M_J planet in $6.9839115^{+0.0000094}_{-0.0000093}$ day orbit around an early G dwarf. Additionally, both planets are on eccentric orbits, ($e = 0.298^{+0.022}_{-0.020}$ for TOI-558 b and $0.151^{+0.012}_{-0.011}$ for TOI-559 b). The measured eccentricities may be remnants from their evolutionary history since tidal forces at these periods would not have had enough time to circularize their orbits. A long-term RV trend suggests the presence of an exterior companion to TOI-559, which we do not detect in high-resolution (∼0.″1) images down to limiting contrast of >5 mag in the red optical. Future efforts should continue RV monitoring to constrain the mass and separation of the stellar or substellar companion. The high mass of both planets is also interesting, and we examine the mass distribution of the current known sample of transiting hot and warm Jupiters. While some tentative trends may be present, further work is warranted. Fortunately, TESS will provide a near magnitude-complete sample of transiting hot Jupiters (Zhou et al. 2019), enabling more robust future studies of the population, possibly yielding signatures of migration. Such future work may help illuminate the evolutionary pathways of hot and warm Jupiters, a question that has persisted since the first exoplanet discoveries.

This research has made use of SAO/NASA's Astrophysics Data System Bibliographic Services. This research has made use of the SIMBAD database, operated at CDS, Strasbourg, France. This work has made use of data from the European Space Agency (ESA) mission Gaia (https://www.cosmos.esa.int/gaia), processed by the Gaia Data Processing and Analysis Consortium (DPAC, https://www.cosmos.esa.int/web/gaia/dpac/consortium). Funding for the DPAC has been provided by national institutions, in particular the institutions participating in the Gaia Multilateral Agreement. This work makes use of observations from the LCOGT network. B.S.G. was supported by a Thomas Jefferson Grant for Space Exploration from the Ohio State State University.

Funding for the TESS mission is provided by NASA's Science Mission directorate. We acknowledge the use of public TESS Alert data from pipelines at the TESS Science Office and at the TESS SPOC. This research has made use of the NASA Exoplanet Archive and the Exoplanet Follow-up Observation Program website, which are operated by the California Institute of Technology, under contract with the National Aeronautics and Space Administration under the Exoplanet Exploration Program. This paper includes data collected by the TESS mission, which are publicly available from the Mikulski Archive for Space Telescopes. Resources supporting this work were provided by the NASA High-End Computing Program through the NASA Advanced Supercomputing Division at Ames Research Center for the production of the SPOC data products. Part of this research was carried out at the Jet Propulsion Laboratory, California Institute of Technology, under a contract with NASA.

This paper includes data gathered with the 6.5 m Magellan Telescopes located at Las Campanas Observatory, Chile. This paper includes observations obtained under Gemini programs GN-2018B-LP-101 and GN-2020B-LP-105. Some of the observations in the paper made use of the High-Resolution Imaging instrument ‘Alopeke. ‘Alopeke was funded by the NASA Exoplanet Exploration Program and built at the NASA Ames Research Center by Steve B. Howell, Nic Scott, Elliott P. Horch, and Emmett Quigley. ‘Alopeke was mounted on the Gemini North telescope of the international Gemini Observatory, a program of NSF’s OIR Lab, which is managed by the Association of Universities for Research in Astronomy under a cooperative agreement with the National Science Foundation on behalf of the Gemini partnership: the National Science Foundation (United States), National Research Council (Canada), Agencia Nacional de Investigación y Desarrollo (Chile), Ministerio de Ciencia, Tecnología e Innovación (Argentina), Ministério da Ciência, Tecnologia, Inovações e Comunicações (Brazil), and Korea Astronomy and Space Science Institute (Republic of Korea).

Facilities: TESS, FLWO 1.5 m (Tillinghast Reflector Echelle Spectrograph), 4.1 m Southern Astrophysical Research (SOAR), LCOGT 0.4 m, LCOGT 1.0 m, 6.5 m Magellan Telescope.

Software: EXOFASTv2 (Eastman et al. 2013; Eastman 2017), AstroImageJ (Collins et al. 2017), Lightkurve (Lightkurve Collaboration et al. 2018), Tesscut (Brasseur et al. 2019), Keplerspline (Vanderburg & Johnson 2014; Shallue & Vanderburg 2018).

ORCID iDs

Mma Ikwut-Ukwa https://orcid.org/0000-0002-4404-5505
Joseph E. Rodriguez https://orcid.org/0000-0001-8812-0565
Samuel N. Quinn https://orcid.org/0000-0002-8964-8377
George Zhou https://orcid.org/0000-0002-4891-3517
Andrew Vanderburg https://orcid.org/0000-0001-7246-5438
Asma Ali https://orcid.org/0000-0001-8431-8793
B. Scott Gaudi https://orcid.org/0000-0003-0395-9869
David W. Latham https://orcid.org/0000-0001-9911-7388
Steve B. Howell https://orcid.org/0000-0002-2532-2853
Chelsea X. Huang https://orcid.org/0000-0003-0918-7484
Allyson Bieryla https://orcid.org/0000-0001-6637-5401
Karen A. Collins https://orcid.org/0000-0001-6588-9574
Theron W. Carmichael https://orcid.org/0000-0001-6416-1274
Markus Rabus https://orcid.org/0000-0003-2935-7196
Jason D. Eastman https://orcid.org/0000-0003-3773-5142
Kevin I. Collins https://orcid.org/0000-0003-2781-3207
Thiam-Guan Tan https://orcid.org/0000-0001-5603-6895
Richard P. Schwarz https://orcid.org/0000-0001-8227-1020
Gordon Myers https://orcid.org/0000-0002-9810-0506
Chris Stockdale https://orcid.org/0000-0003-2163-1437
John F. Kielkopf https://orcid.org/0000-0003-0497-2651
Don J. Radford https://orcid.org/0000-0002-3940-2360
Ryan J. Oelkers https://orcid.org/0000-0002-0582-1751
Jon M. Jenkins https://orcid.org/0000-0002-4715-9460
George R. Ricker https://orcid.org/0000-0003-2058-6662
Sara Seager https://orcid.org/0000-0002-6892-6948
Roland K. Vanderspek https://orcid.org/0000-0001-6763-6562
Joshua N. Winn https://orcid.org/0000-0002-4265-047X
Jennifer Burt https://orcid.org/0000-0002-0040-6815
R. Paul Butler https://orcid.org/0000-0003-1305-3761
Michael L. Calkins https://orcid.org/0000-0002-2830-5661
Jeffrey D. Crane https://orcid.org/0000-0002-5226-787X
Crystal L. Gnilka https://orcid.org/0000-0003-2519-6161
Gilbert A. Esquerdo https://orcid.org/0000-0002-9789-5474
William Fong https://orcid.org/0000-0003-0241-2757
Laura Kreidberg https://orcid.org/0000-0003-0514-1147
Jessica Mink https://orcid.org/0000-0003-3594-1823
David R. Rodriguez https://orcid.org/0000-0003-1286-5231
Joshua E. Schlieder https://orcid.org/0000-0001-5347-7062
Avi Shporer https://orcid.org/0000-0002-1836-3120
Eric B. Ting https://orcid.org/0000-0002-8219-9505
Daniel A. Yahalomi https://orcid.org/0000-0003-4755-584X

References

Adams, F. C., & Laughlin, G. 2006, ApJ, 649, 1004
Bailey, E., & Batygin, K. 2018, ApJL, 866, L2
Batygin, K., Bodenheimer, P. H., & Laughlin, G. P. 2016, ApJ, 829, 114
Beaugé, C., & Nesvorný, D. 2012, ApJ, 751, 119
Bensby, T., Feltzing, S., & Oey, M. S. 2014, A&A, 562, A71
Bodenheimer, P., & Pollack, J. B. 1986, Icar, 67, 391
Bovy, J. 2017, MNRAS, 470, 1360
Brahm, R., Jordán, A., & Espinoza, N. 2017, PASP, 129, 034002
Brasseur, C. E., Phillip, C., Fleming, S. W., Mullally, S. E., & White, R. L. 2019, Astrocut: Tools for Creating Cutouts of TESS Images, Astrophysics Source Code Library, ascl:1905.007
Brown, T. M., Baliber, N., Bianco, F. B., et al. 2013, PASP, 125, 1031
Buchhave, L. A., Bakos, G. Á, Hartman, J. D., et al. 2010, ApJ, 720, 1118
Buchhave, L. A., Latham, D. W., Johansen, A., et al. 2012, Natur, 486, 375
Burt, J. A., Nielsen, L. D., Quinn, S. N., et al. 2020, AJ, 160, 153
Butler, R. P., Marcy, G. W., Williams, E., et al. 1996, PASP, 108, 500
Choi, J., Dotter, A., Conroy, C., et al. 2016, ApJ, 823, 102
Ciardi, D. R., Beichman, C. A., Horch, E. P., & Howell, S. B. 2015, ApJ, 805, 16
Coşkunoǧlu, B., Ak, S., Bilir, S., et al. 2011, MNRAS, 412, 1237
Collins, K. A., Kielkopf, J. F., Stassun, K. G., & Hessman, F. V. 2017, AJ, 153, 77
Crane, J. D., Shectman, S. A., & Butler, R. P. 2006, Proc. SPIE, 7014, 626931
Crane, J. D., Shectman, S. A., Butler, R. P., et al. 2010, Proc. SPIE, 7735, 773553
Crane, J. D., Shectman, S. A., Butler, R. P., Thompson, I. B., & Burley, G. S. 2008, Proc. SPIE, 7014, 701479
Cutri, R. M., Skrutskie, M. F., van Dyk, S., et al. 2003, yCat, 2246, 0
Cutri, R. M., Wright, E. L., Conrow, T., et al. 2012, VizieR On-line Data Catalog, II, 311
Dawson, R. I., & Johnson, J. A. 2018, ARA&A, 56, 175
Donati, J.-F., Semel, M., Carter, B. D., Rees, D. E., & Collier Cameron, A. 1997, MNRAS, 291, 658
Dotter, A. 2016, ApJS, 222, 8
Eastman, J. 2017, EXOFASTv2: Generalized Publication-quality Exoplanet Modeling Code, Astrophysics Source Code Library, ascl:1710.003
Eastman, J., Gaudi, B. S., & Agol, E. 2013, PASP, 125, 83
Eastman, J. D., Rodriguez, J. E., Agol, E., et al. 2019, arXiv:1907.09480
Fabrycky, D., & Tremaine, S. 2007, ApJ, 669, 1298
Fűrész, G. 2008, PhD thesis, University of Szeged, Hungary
Fulton, B. J., & Petigura, E. A. 2018, AJ, 156, 264
Fulton, B. J., Petigura, E. A., Howard, A. W., et al. 2017, AJ, 154, 109
Gagné, J., Mamajek, E. E., Malo, L., et al. 2018, ApJ, 856, 23
Gaia Collaboration, Brown, A. G. A., Vallenari, A., et al. 2018, A&A, 616, A1
Gaudi, B. S., Seager, S., & Mallen-Ornelas, G. 2005, ApJ, 623, 472
Goldreich, P., & Tremaine, S. 1980, ApJ, 241, 425
Grover, N. B. 1977, Comp. Prog. Biomed., 7, 247
Høg, E., Fabricius, C., Makarov, V. V., et al. 2000, A&A, 355, L27
Howell, S. B., Everett, M. E., Sherry, W., Horch, E., & Ciardi, D. R. 2011, AJ, 142, 19
Huang, C. X., Vanderburg, A., Pál, A., et al. 2020, RNAAS, 4, 206
Husser, T. O., Wende-von Berg, S., Dreizler, S., et al. 2013, A&A, 553, A6
Jackson, B., Barnes, R., & Greenberg, R. 2009, ApJ, 698, 1357

Jenkins, J. M. 2002, ApJ, 575, 493
Jenkins, J. M., Twicken, J. D., McCauliff, S., et al. 2016, Proc. SPIE, 9913, 99133E
Jensen, E. 2013, Tapir: A Web Interface for Transit/Eclipse Observability, Astrophysics Source Code Library, ascl:1306.007
Kovács, G., Zucker, S., & Mazeh, T. 2002, A&A, 391, 369
Li, J., Tenenbaum, P., Twicken, J. D., et al. 2019, PASP, 131, 024506
Lightkurve Collaboration, Cardoso, J. V. D. M., Hedges, C., et al. 2018, Lightkurve: Kepler and TESS Time Series Analysis in Python, Astrophysics Source Code Library, ascl:1812.013
Lin, D. N. C., Bodenheimer, P., & Richardson, D. C. 1996, Natur, 380, 606
Lin, D. N. C., & Papaloizou, J. 1986, ApJ, 309, 846
Lindegren, L., Hernández, J., Bombrun, A., et al. 2018, A&A, 616, A2
Lopez, E. D., & Fortney, J. J. 2013, ApJ, 776, 2
Mackereth, J. T., & Bovy, J. 2018, PASP, 130, 114501
Madhusudhan, N., Amin, M. A., & Kennedy, G. M. 2014, ApJL, 794, L12
Massey, F. J. 1951, J. Am. Stat. Assoc., 46, 68
Matsakos, T., & Königl, A. 2016, ApJL, 820, L8
Moe, M., & Kratter, K. M. 2019, arXiv:1912.01699
Murray-Clay, R. A., Chiang, E. I., & Murray, N. 2009, ApJ, 693, 23
Nagasawa, M., & Ida, S. 2011, ApJ, 742, 72
Naoz, S., Farr, W. M., Lithwick, Y., Rasio, F. A., & Teyssandier, J. 2011, Natur, 473, 187
Nielsen, L. D., Brahm, R., Bouchy, F., et al. 2020, A&A, 639, A76
Owen, J. E., & Jackson, A. P. 2012, MNRAS, 425, 2931
Paxton, B., Bildsten, L., Dotter, A., et al. 2011, ApJS, 192, 3
Paxton, B., Cantiello, M., Arras, P., et al. 2013, ApJS, 208, 4
Paxton, B., Marchant, P., Schwab, J., et al. 2015, ApJS, 220, 15
Pecaut, M. J., & Mamajek, E. E. 2013, ApJS, 208, 9
Pepper, J., Kane, S. R., Rodriguez, J. E., et al. 2020, AJ, 159, 243
Piso, A.-M. A., Youdin, A. N., & Murray-Clay, R. A. 2015, ApJ, 800, 82
Pollack, J. B., Hubickyj, O., Bodenheimer, P., et al. 1996, Icar, 124, 62
Quinn, S. N., White, R. J., Latham, D. W., et al. 2012, ApJL, 756, L33
Rafikov, R. R. 2006, ApJ, 648, 666
Rasio, F. A., & Ford, E. B. 1996, Sci, 274, 954
Ricker, G. R., Winn, J. N., Vanderspek, R., et al. 2015, JATIS, 1, 014003
Rodriguez, J. E., Eastman, J. D., Zhou, G., et al. 2019b, AJ, 158, 197
Rodriguez, J. E., Quinn, S. N., Huang, C. X., et al. 2019a, AJ, 157, 191
Rodriguez, J. E., Quinn, S. N., Zhou, G., et al. 2021, AJ, 161, 194
Schlafly, E. F., & Finkbeiner, D. P. 2011, ApJ, 737, 103
Schlaufman, K. C. 2015, ApJL, 799, L26
Schlaufman, K. C. 2018, ApJ, 853, 37
Schlegel, D. J., Finkbeiner, D. P., & Davis, M. 1998, ApJ, 500, 525
Scholz, F. W., & Stephens, M. A. 1987, J. Am. Stat. Assoc., 82, 918
Shallue, C. J., & Vanderburg, A. 2018, AJ, 155, 94
Smith, J. C., Stumpe, M. C., Van Cleve, J. E., et al. 2012, PASP, 124, 1000
Stassun, K. G., Oelkers, R. J., Pepper, J., et al. 2018, AJ, 156, 102
Stumpe, M. C., Smith, J. C., Catanzarite, J. H., et al. 2014, PASP, 126, 100
Teske, J., Xuesong Wang, S., Wolfgang, A., et al. 2021, ApJS, 256, 33
Tian, F., Toon, O. B., Pavlov, A. A., & De Sterck, H. 2005, ApJ, 621, 1049
Tokovinin, A. 2018, PASP, 130, 035002
Tokovinin, A., Fischer, D. A., Bonati, M., et al. 2013, PASP, 125, 1336
Twicken, J. D., Catanzarite, J. H., Clarke, B. D., et al. 2018, PASP, 130, 064502
Vanderburg, A., & Johnson, J. A. 2014, PASP, 126, 948
Vanderburg, A., Latham, D. W., Buchhave, L. A., et al. 2016, ApJS, 222, 14
Vanderburg, A., Huang, C. X., Rodriguez, J. E., et al. 2019, ApJL, 881, L19
Wu, Y., & Lithwick, Y. 2011, ApJ, 735, 109
Wu, Y., & Murray, N. 2003, ApJ, 589, 605
Yelle, R. V. 2004, Icar, 170, 167
Zhou, G., Huang, C. X., Bakos, G. Á., et al. 2019, AJ, 158, 141
Zhou, G., Quinn, S. N., Irwin, J., et al. 2021, AJ, 161, 2
Zhou, G., Rodriguez, J. E., Vanderburg, A., et al. 2018, AJ, 156, 93
Ziegler, C., Law, N. M., Baranec, C., et al. 2018, AJ, 155, 161
Ziegler, C., Tokovinin, A., Briceño, C., et al. 2020, AJ, 159, 19
Zinn, J. C., Pinsonneault, M. H., Huber, D., et al. 2019, ApJ, 885, 166